Article

J. Biol. Regul. Homeost. Agents. 2024; 38(5): 4153–4170
https://doi.org/10.23812/j.biol.regul.homeost.agents.20243805.330

Novel Quinazoline Derivative Activates FIH-1 in MCF-7 Cells and 7, 12-Dimethylbenz[a]-Anthracene Induced Mammary Gland Carcinoma in Albino Rats

Soniya Rani[1], Mohd Nazam Ansari[2], Abdulaziz S. Saeedan[2], Gaurav Kaithwas[1,*]

[1]Department of Pharmaceutical Sciences, Babasaheb Bhimrao Ambedkar University (A Central University), 226 025 Lucknow, India
[2]Department of Pharmacology and Toxicology, College of Pharmacy, Prince Sattam Bin Abdulaziz University, 11942 Al-Kharj, Saudi Arabia
*Correspondence: gauravpharm@hotmail.com (Gaurav Kaithwas)
Published: 1 May 2024

Background: Mammary gland carcinoma is a solid tumor with a hypoxic core due to oxygen deficiency. Factor inhibiting hypoxia-inducible factor-1α (FIH-1) is an oxygen sensor that becomes inactive in a hypoxic environment, making it unable to regulate rapidly proliferating cancer cells. Thus, we hypothesize that the chemical activation of FIH-1 could be a novel mechanism for regulating mammary gland carcinoma. In this study, 6-(5,11-dioxoisoindolo [2,1-a] quinazolin-6(5H,6aH,11H)-yl)-N-(1H-imidazol-2-yl) hexanamide (BBAP-9) was investigated for its anticancer potential.

Methods: A library of 67,609 drug-like molecules was virtually screened against FIH-1 based on Lipinski's rule from the ZINC database. BBAP-9 was selected as a potent FIH-1 activator through docking study, absorption, distribution, metabolism, excretion and toxicity (ADMET) profile, and *in vitro* 2-oxoglutarate dependent FIH-1 activation assay. Further, its *in vitro* cytotoxicity and apoptotic activity were scrutinized against MCF-7 cells using acridine orange/ethidium bromide (AO/EB) and 5,5,6,6′-tetrachloro- 1,1′,3,3′-tetraethylbenzimi-dazoylcarbocyanine iodide (JC-1) stainings and its *in vivo* activity against 7,12-dimethylbenz[a]anthracene (DMBA) induced mammary gland carcinoma in Wistar rats by performing various parameters such as hemodynamic, carmine-alum staining, histology, scanning electron microscopy, and biochemical analysis.

Results: Our results demonstrated that BBAP-9 showed a good docking score (–8.162) and a suitable ADMET profile. BBAP-9 activated FIH-1 when scrutinized through a 2-oxoglutarate dependent assay ($p < 0.05$). BBAP-9 exhibited significant cytotoxicity with half-maximal inhibitory concentration (IC50) of 16.9 $\pm$ 0.85 µM ($p < 0.05$) and induced apoptotic changes in MCF-7 cells, as revealed by AO/EB ($p < 0.05$) and JC-1 stainings ($p < 0.05$). Once scrutinized against DMBA-induced mammary gland carcinoma, BBAP-9 restored autonomic dysfunction ($p < 0.05$), tissue vascularization, morphological architecture, membrane ruffles, and oxidative stress markers [thiobarbituric acid reactive substances (TBARs), protein carbonyl (PC), glutathione (GSH), super oxide dismutase (SOD), and catalase)] toward normal control ($p < 0.05$).

Conclusions: Overall, the current study's findings demonstrate that BBAP-9 has significant cytotoxicity and apoptotic activity against MCF-7 cells. Moreover, BBAP-9 has chemotherapeutic efficacy on DMBA-induced mammary gland carcinoma, which can be attributed to its propensity to enhance antioxidant profiles and inhibit cellular proliferation, improve surface architecture, soothing membrane ruffles, and decrease lactate effects. Thus, we postulated that BBAP-9 may be a novel FIH-1 activator in mammary gland carcinoma.

Keywords: apoptosis; BBAP-9; cancer; factor inhibiting HIF-1α; MCF-7

Introduction

Mammary gland carcinoma is the second most frequent cancer among women worldwide, with an increasing incidence. According to epidemiological reports, the number of cases of mammary gland carcinoma worldwide is expected to reach approximately 2 million by 2030 [1]. In India, the National Cancer Registry Programme (NCRP) reported 0.15 million new cases and 76,000 fatalities from mammary gland carcinoma.

Mammary gland carcinoma is a solid tumor and the core is hypoxic due to oxygen deficiency. Studies have linked hypoxia to metastasis initiation, drug resistance, and aggressive behavior of cancer cells [2–4]. Young *et al.* [5] demonstrated that hypoxia affects cancer cell behavior, with two-fold higher metastatic efficiency in hypoxia-treated cells. Vaupel *et al.* [6] reported that hypoxia is a prognostic factor for tumor growth and development in various malignancies. Hypoxia-inducible factors (HIFs) are thoroughly studied mechanisms of cancer cell adaptation in hypoxic microenvironments. Among the various HIF transcriptional factors, hypoxia-inducible factor-1alpha (HIF-1α) is the foremost transcription factor stabilized in the hypoxic environment and transmits signals for cancer pro-

Journal of
BIOLOGICAL REGULATORS
and Homeostatic Agents

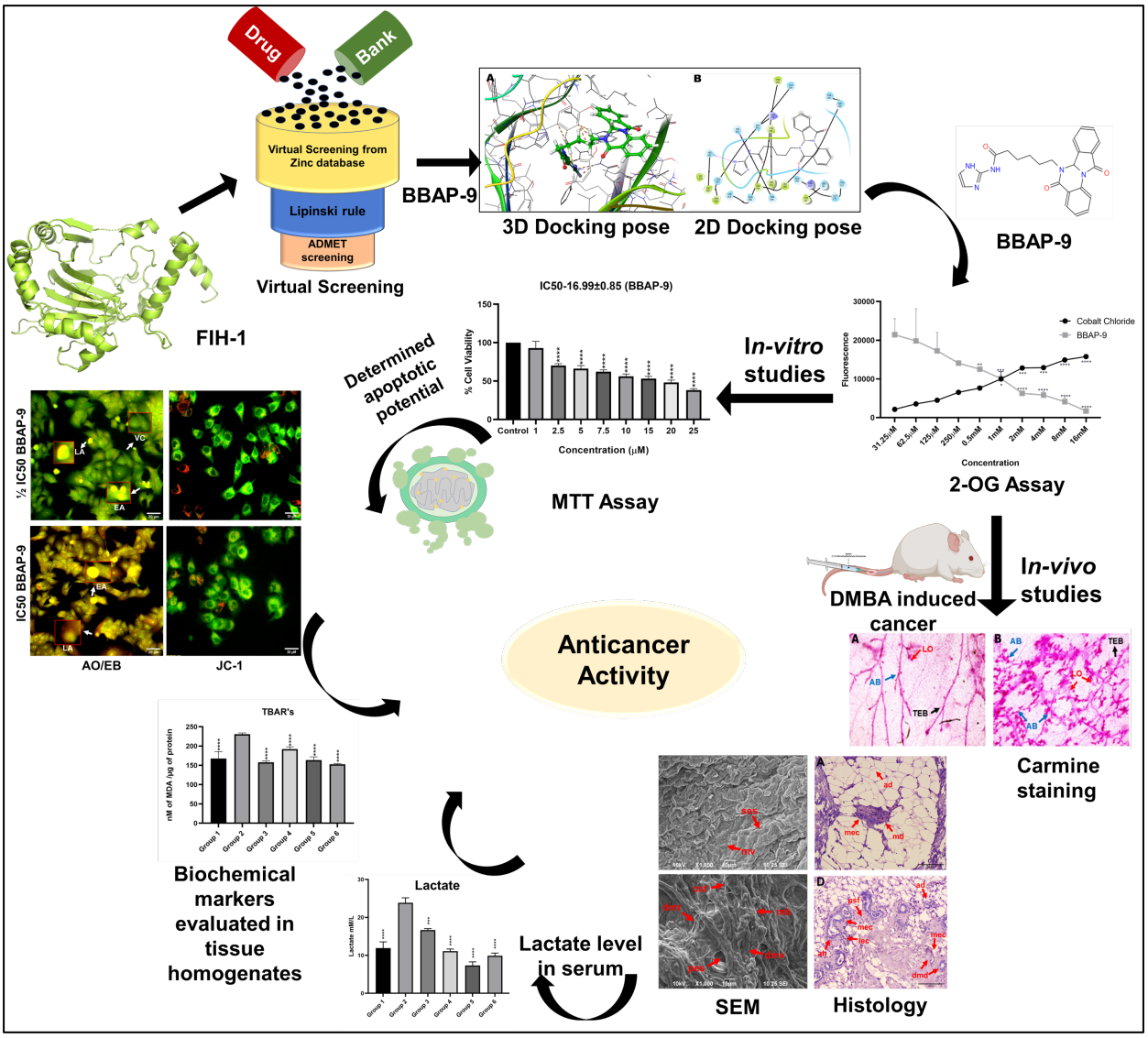

Graphical Abstract

liferation and survival [7]. Prolyl hydroxylase-2 (PHD-2) and factor inhibiting hypoxia-inducible factor-1α (FIH-1) are oxygen sensors, and homodimeric proteins having 244 and 351 amino acid residues, respectively [8]. PHD-2 and FIH-1 control the transcriptional activity of HIF-1α through oxygen-dependent hydroxylation at the Proline (Pro 402 and 564) and asparagine (Asn803) residue of N-terminal transactivation domain (N-TAD) and C-terminal transactivation domain (C-TAD) of HIF-1α, respectively. Low oxygen hypoxic conditions can restrict PHD-2 and FIH-1 activity consequently HIF-1α is transcriptionally activated in hypoxic solid tumors [9]. Given the above, our laboratory has screened and reported several small chemical entities as PHD-2 activators to regulate HIF-1α with significant anticancer potential in mammary gland carcinoma [10–12].

FIH-1 regulates the transcriptional activity of HIF-1α even at minimal intracellular oxygen concentration compared with PHD-2. More precisely, FIH-1 is a better sensor for intracellular oxygen concentration than PHD-2. Accordingly, FIH-1 can be considered a better regulator of the transcriptional activity of HIF-1α and consequent mechanisms of angiogenesis and metastasis [13–15]. Overall, FIH-1 plays a significant role in cancer biology by regulating transcription of HIF-1α.

Considering the above, we hypothesize that chemical activation of FIH-1 could be a better and novel mechanism to regulate the transcriptional activity of HIF-1α. Consequently, the present study was designed to screen and evaluate potential activators of FIH-1 in mammary gland carcinoma.

Materials and Methods

6-(5,11-dioxoisoindolo[2,1-a]-quinazolin-6(5H,6aH, 11H)-yl)-N-(1H-imidazol-2-yl) hexanamide (BBAP-9) was procured from Eximed Laboratory, Kyiv, Ukraine (catalogue no. EiM08-38511, customer ID: 16255). Tamoxifen (TAM) was received as a gift sample from Hiral Labs Ltd.,

Roorkee, UK, India. The other materials included dulbecco modified eagle's media (DMEM, 11965092, Gibco, Grand Island, NY, USA); fetal bovine serum (FBS, 10270106, Gibco, Grand Island, NY, USA); trypsin (25200072, Gibco, Grand Island, NY, USA); dulbecco phosphate buffered saline (DPBS, 14200075, Gibco, Grand Island, NY, USA); acridine orange (AO, MB116, Himedia, Thane, MH, India); ethidium bromide (EB, MB071, Himedia, Thane, MH, India); 5,5,6,6′-tetrachloro-1,1′,3,3′-tetraethylbenzimi-dazoylcarbocyanine iodide (JC-1) assay kit (M34152, Thermo Scientific, Waltham, MA, USA); 3-(4,5-dimethylthiazol-2-yl)-2,5-diphenyltetrazolium bromide (MTT, TC191, Himedia, Thane, MH, India); antibiotic-antimycotic (100X) (15140122, Gibco, Grand Island, NY, USA); eosin (S007, Himedia, Thane, MH, India); Haematoxylin (S058, Himedia, Thane, MH, India); dimethyl sulfoxide (DMSO, D1435, Sigma Aldrich, Saint Louis, MO, USA); and 7,12-dimethylbenz[a]anthracene (DMBA, D3254, Sigma Aldrich, Saint Louis, MO, USA). All other chemicals were of molecular grade and obtained from Genetix Biotech Asia Pvt. Ltd., NDL, DL, India.

In-Silico Study

Protein Preparation

The Protein Data Bank (PDB ID-5OP6) 3D crystal structure of the FIH-1 protein was obtained (https://www.rcsb.org/structure/5OP6). The Protein Preparation Wizard in the Schrodinger Suite was used to construct the FIH-1 protein (Schrodinger Release 2021-1). During protein preprocessing, hydrogen atoms were checked, hydrogen bonds were optimized, atomic collisions were eliminated, disulfide bonds were formed, and formal charges were added to the hetero groups in the atoms and molecules. Water molecules larger than 5 nm were removed from the hetero groups. The possible ionization states of the protein structure were generated using Epik, and the most stable state was selected. We also used Prime from the Schrödinger Suite to complete the missing chains and loops. The sample water orientation was then enhanced, and protonation states at a neutral pH were produced using PROPKA (https://www.ddl.unimi.it/vegaol/propka.htm). The OPLS3e force field was then used in controlled minimization to obtain heavy atoms with a Root Mean Square Deviation value of 0.30. This structure was further used in bioinformatics studies [16].

Ligand Preparation

The structural data file (SDF) format of the Interbiosciences (IBS) library was obtained from the ZINC database. The library was filtered using Lipinski's principle. The Ligand Preparation (LigPrep) module was used to prepare the ligands (pH 7.0 ± 2.0). The stereoisomers and chiralities of the ligands were acquired for high-throughput virtual screening [17].

Virtual Screening

Virtual screening is a computer-based technique used in drug discovery to search libraries of small compounds to identify structures most likely to bind to a drug target. A library of 67,609 chemical compounds was downloaded from the ZINC database (https://zinc.docking.org/). Virtual screening of the ZINC database was performed against the target protein FIH-1. Screening for the best lead molecules was performed using the Glide module of Schrodinger via high-throughput virtual screening (HTVS) and further followed by the standard precision (SP) module program [17,18].

Molecular Docking and Binding Energy Calculation

The Schrodinger Suite Glide program conducted molecular docking and virtual screening. The Receptor grid-generating application of Glide used the energy-minimized FIH-1 structure from PrepWizard for grid generation. After grid construction, the glide docking methodology was followed using a grid file and a minimized ligand library. The Glide dock and docking score in the pose viewer file format determined the top hits based on receptor affinity. Subsequently, the pose viewer file binding energy was estimated using molecular mechanics-generalized born surface area (MM-GBSA) and calculated in ΔG-Kcal/mol [17,18].

ADME Profiling

ADME characteristics were examined using the QikProp tool. The tool predicts physicochemical characteristics such as molecular weight, partition coefficient, hydrogen bond acceptors, donors, Lipinski's rule, human oral absorption, blood-brain barrier, metabolism, and LogK human serum albumin [16,18].

Toxicity Estimation Software Tool (TEST)

TEST is a computational tool for determining chemical compounds toxicity and mutagenicity index (https://www.epa.gov/chemical-research/toxicity-estimation-software-tool-test). The screened compounds were tested for their toxicity and mutagenicity profiles [10].

In Vitro FIH-1 Activation Assay (2-Oxoglutarate (2-OG) Dependent Assay)

FIH-1 activity was determined by 2-OG dependent assay using a method previously established in our laboratory with slight modifications. The serum samples were taken from control albino Wistar rats and mixed with five volumes of 0.25M dextrose (TC130, Himedia, Thane, MH, India); comprising HEPES (H3537, Sigma Aldrich, Saint Louis, MO, USA) (50 mM, pH 7.0) buffer. Thereafter, the above mixture was added with various concentrations of test compounds (BBAP-9 and $COCl_2$), PMSF (329-98-6, Sigma Aldrich, Saint Louis, MO, USA) (50 µg/mL), 1 mM DTT (R0861, Thermo Scientific, Waltham, MA, USA), 1000

Journal of
BIOLOGICAL REGULATORS
and Homeostatic Agents

μM EDTA (60-00-4, Loba Chemie, Colaba, MUM, India), and 0.1% Triton X100 (9002-93-1, Genetix Biotech, NDL, DL, India), followed by centrifugation, and the supernatant was collected. Subsequently, the supernatant (100 μL) and 990 μL of FIH-1 activation buffer were mixed at 30 °C for 3 h. 100 μL 0.5M HCl (311350222BT, Finar, Ahmedabad, GUJ, India) was added to terminate the reaction, and 50 μL of o-phenylenediamine (P9029-50G, Sigma Aldrich, Saint Louis, MO, USA) (10 mg/mL prepared in 0.5M HCl, 311350222BT, Finar, Ahmedabad, GUJ, India) was added to achieve derivatization. After heating at 95 °C for 10 min, the reaction mixture was centrifuged at 10,000 rpm for 5 min, and the supernatant was collected. Finally, 100 μL of supernatant was combined with 60 μL of 1.2 M sodium hydroxide, and fluorescence was assessed using a spectrofluorometer (Carry Eclipse Fluorescence Spectrophotometer, 18073115, Agilent Technology, Santa Clara, CA, USA) at 340 nm excitation and 420 nm emission wavelengths. The activity of FIH-1 depends on the 2-OG level. The level of 2-OG present in the sample is closely related to the fluorescence intensity; less fluorescence intensity indicates less 2-OG level which reflects higher FIH-1 activity, and vice versa. Three different groups were used for this test, including the control group (serum), the negative control group (serum + $COCl_2$), and the positive control group (serum + BBAP-9). The level of FIH-1 activity in the control group was considered to be 100% to assess the activity of BBAP-9 and $COCl_2$ [10,19,20].

In Vitro Study

Cell Line and Its Culture

MCF-7 cells were retrieved from the National Centre for Cell Sciences (NCCS), Pune, MH, India (Authentication no. 997/2021-22). The cell lines received from NCCS, Pune were authenticated for the absence of mycoplasma contamination and were tested for short tandem repeat (STR) analysis on sixteen STR loci. The cells were cultured in DMEM medium supplemented with 10% FBS and 1% antibiotic-antimycotic solution under humidified conditions at 37 °C with 5% CO_2 [21].

MTT Assay

Briefly, MCF-7 cells (1×10^5) were plated in 96-well plates and treated with increasing concentrations of BBAP-9 and TAM (1, 5, 10, 15, 20, and 25 μM) for 24 h, respectively. Thereafter, the medium was aspirated, MTT was added, and fresh medium was incubated for 4 h. Purple-colored formazans were formed, and the absorbance was measured using a microplate reader (SpectraMax ABS Plus, Rochester, NY, USA) at 570 nm. Cell viability was evaluated as a percentage of cytoprotection compared with the control group, which was set to 100%. The color formation is directly correlated to the viability of the cells [21]. The following formula was used to determine the cell viability:

$$\%\,\text{Cell Viability} = \frac{\text{Absorbance of treated cells} - \text{Absorbance of blank}}{\text{Absorbance of control cells} - \text{Absorbance of blank}} \times 100$$

Apoptotic Morphological Study Using Acridine Orange/Ethidium Bromide (AO/EB) Dye

MCF-7 cells (1×10^6) were seeded in 6-well plates, treated with BBAP-9 and TAM for 24 h. The cells were stained with AO (100 μg/mL) (MB116, Himedia, Thane, MH, India) and EB (MB071, Himedia, Thane, MH, India) (100 μg/mL) (1:1) and incubated for 5 min. After incubation, cells were washed and visualized under a fluorescence microscope at 20× magnification (IX 53, Olympus, Shinjuku, Tokyo, Japan). The viable cells display a green colour, early apoptotic cells show a yellow colour, and late apoptotic cells represent an orange colour. Quantification of viable, early, and late apoptotic cells, according to the percentage of apoptotic cells was determined by [% of apoptotic cells = (total number of apoptotic cells/total number of cells counted) × 100] [21–23].

Measurement of Mitochondrial Membrane Potential (MMP) Using JC-1

MCF-7 cells (1×10^6) were plated in 6-well plates, treated with BBAP-9 and TAM for 24 h. Subsequently, the medium was aspirated, washed thrice with PBS, and treated with JC-1 dye (2 μM) in the dark for 30 min. Finally, stained cells were examined under a fluorescence microscope at 20× magnification (IX 53, Olympus, Shinjuku, Tokyo, Japan) [10,23].

In Vivo Study

Animals and Experimental Design

This study used female Wistar albino rats (5–6 weeks old and 100–150 g body weight). The animals were maintained in the propylene cages in six groups under standard conditions with a 12 h dark-light cycle. The animals were free to access animal diet and water *ad libitum*. Animals were acclimated for 15–20 days; the animals were randomly allocated into six groups of six animals each. The protocols were also authorized and performed following the guidelines laid by the Committee for Control and Supervision of Experiments on Animals (CCSEA) (Approval No. UIP/IAEC/Nov.-2019/13). The designed study protocol is specified in **Supplementary Table 1**. The carcinogen was administered by a single intravenous injection of DMBA followed by oral administration of BBAP-9 therapy for 15 days [23–25]. Hemodynamic changes were noted after the completion of the study, and the next day the blood sample was withdrawn and centrifuged to obtain serum. The animals were dissected under anesthesia using a combination of ketamine hydrochloride (55150-438-01, Auromedics, Windsor, NJ, USA) (100 mg/kg, i.m.) and diazepam (69339-136-34, Dash, saddler, NJ, USA) (5 mg/kg

i.m.); followed by cervical decapitation. The mammary gland tissues were extracted, preserved at –20 °C, and subjected to further estimations.

Hemodynamic Changes

Animals were anesthetized with ketamine hydrochloride (100 mg/kg, i.m.) and diazepam (5mg/kg, i.m.) for electrocardiogram (ECG) and heart rate variability (HRV) analysis using a method previously established in our laboratory. The ECG and HRV signals were recorded and analysed using Lab Chart Pro-8 software (AD Instruments, Bella Vista, New South Wales, Australia). Further, the data were analyzed using MetaboAnalyst 5.0 (https://www.metaboanalyst.ca/). [24].

Carmine Staining

The mammary gland tissue from each animal was separated and stretched onto a slide. The slides were immersed overnight in Carnoy's fixative [solution of 60% ethanol (64-17-5, Thermo Fisher Scientific, Waltham, MA, USA), 30% chloroform (572140223LS, Finar, Ahmedabad, GUJ, India), and 10% glacial acetic acid (64-19-7, Thermo Fisher Scientific, Waltham, MA, USA)]. Thereafter, the tissues were hydrated with decreasing ethanol concentrations (90%, 70%, 35%, and 15%) and stained with carmine alum solution [0.2% carmine (TC264, Himedia, Thane, MH, India) mixed with 0.5% aluminium potassium sulfate (7784-24-9, Loba Chemie, Colaba, MUM, India)]. The stained slides were dehydrated using increasing concentrations of ethanol (70%, 95%, and 100%) and then immersed in xylene for overnight. The slides were observed under a microscope (IX 53, Olympus, Shinjuku, Tokyo, Japan) at 4× magnification to examine the proliferation of alveolar buds (AB), terminal end buds (TEB), lobules (LO), and differentiation score (DF score) [10,23].

Hematoxylin and Eosin (H&E) Staining

Tissues from the mammary glands were preserved in 10% formalin, dehydrated, and embedded in paraffin. They were cut into 5 µm slices and stained with H&E. The tissues were examined under microscope and appraised to assess the cellular architectures such as luminal epithelial cells (lec), myoepithelial cells (mec), mammary ducts (md), and adipocytes (ad) in mammary tissues at 4× magnification (IX 53, Olympus, Shinjuku, Tokyo, Japan) [10,24].

Scanning Electron Microscopy (SEM) Analysis

The surface architecture of mammary gland tissues was examined by SEM using HCl-collagenase and enzymatic-dependent digestion method. The small mammary gland tissue sections were cut and digested at 37 °C using hanks balanced salt solution (HBSS); comprising 100 µg/mL collagenase II (TC212-100MG, Himedia, Thane, MH, India) and 2.5 turbidity reducing unit (TRU) of hyaluronidase (37326-33-3, MP Biochemicals, Santa Ana, CA, USA). The tissues were rinsed twice with HBSS before fixation for 3 h at room temperature with 4% glutaraldehyde (111-30-8, Loba Chemie, Colaba, MUM, India) in 0.1M cacodylate/HCl buffer (6131-99-3, Sigma Aldrich, Saint Louis, MO, USA) (pH 7.2). The post-fixation step was performed using 1% osmium tetroxide. The tissue samples were immersed for 30 min in 8 N HCl at 60 °C. Following HCl digestion, tissue samples were washed thrice with distilled water to eliminate the acid. Increasing concentrations of acetone (70%, 80%, 90%, and 100%) were used to dry the samples. All samples were dried, dehydrated by acetone using the critical point technique, processed with platinum coating, and observed under SEM (X1000) (JEOL JSM-6490LV, Mitaka, Tokyo, Japan) [10,26].

Biochemical Markers

Samples were thawed, weighed (10% w/v), and homogenized in 0.15M KCl (7447-40-7, Loba Chemie, Colaba, MUM, India). After centrifuging the homogenates, the supernatant was collected and stored at –20 °C for biochemical estimations. The biochemical parameters such as thiobarbituric acid reactive substances (TBARs), protein carbonyl (PC), super oxide dismutase (SOD), glutathione (GSH), and catalase were performed using the below methods established at our laboratory [24,27].

TBARs Estimation. Mammary gland tissue homogenate (10%), 0.5 M trichloro acetic acid (TCA, 30%), and 0.5 M thiobarbituric acid (TBA, 0.8%) were taken in a microcentrifuge tube and mixed by shaking in a water bath at 80 °C for 30 min (covered with aluminium foil). After that, the tubes were kept in ice-cold water for 15 min. The tissue homogenates were precipitated by centrifugation at 3000 rpm for 15 min, and the supernatant was separated. A microplate reader measured (SpectraMax ABS Plus, Rochester, NY, USA) the absorbance at 540 nm [28]. The following formula was used to estimate malonaldehyde (MDA) levels:

$$\text{Nm of MDA/mg of protein} = \frac{\text{V} \times \text{OD at } 540 \text{ nm}}{0.56 \times \text{ protein concentration}}$$

where V is the final volume of the test solution.

PC Estimation. Mammary gland tissue homogenate (150 µL, 10%) was precipitated using 500 µL TCA (10%) and centrifuged at 13,000 rpm for 2 min. After that, the supernatant was removed and pellets were incubated with 250 µL of 0.2% 2,2-diphenyl-1-picryl hydrazyl (1898-66-4, Sigma Aldrich, Saint Louis, MO, USA) for 1 h with constant vortexing at 5 min intervals. Again, the pellets were precipitated using 50 µL TCA (100%), vortexed, centrifuged (13,000 rpm for 5 min) and the supernatant was removed entirely from the tubes. The pellets were rinsed with 500 µL of ethanol: ethyl acetate (1:1) mixture thrice. Finally, 300 µL of 6M guanidine hydrochloride (50-01-1, Sigma Aldrich, Saint Louis, MO, USA) was added to dissolve the

Journal of
BIOLOGICAL REGULATORS
and Homeostatic Agents

pellets, and absorbance was measured at 360 nm using a microplate reader (SpectraMax ABS Plus, Rochester, NY, USA) [28].

Estimation of the SOD. 10% mammary tissue homogenate was prepared in tris-HCl buffer (1185-53-1, Loba Chemie, Colaba, MUM, India) (pH 8.5). The 100 µL of tissue homogenate was taken in a test tube and the volume was made up to 3 mL with tris-HCl buffer. Further, 25 µL of pyrogallol was added and changes in absorbance were measured at 420 nm at one-min intervals for 3 min. The absorbance changed at 420 nm in the presence of pyrogallol and was inhibited in the presence of SOD. 50% inhibition of pyrogallol auto-oxidation per 3 mL of assay mixture and is given by the following formula:

$$\text{Unit of SOD/mg of protein} = 100 \times \frac{(A-B)}{(A \times 50)} / \text{mg of protein}$$

where A = change in absorbance per min in control and B = change in absorbance per min in the test sample [27,28].

Estimation of Catalase. 10% mammary gland tissue homogenate was prepared in potassium phosphate buffer (7778-77-0, Sigma Aldrich, Saint Louis, MO, USA) (50 mM) and centrifuged at 10,000 rpm for 20 min. 50 µL of supernatant and 2.95 mL of H_2O_2 (7722-84-1, Loba Chemie, Colaba, MUM, India) (19 mM in same buffer) were taken and the disappearance of H_2O_2 was examined at 1 min intervals for 3 min at 240 nm [28].

The following formula was used to calculate tissue catalase activity:

$$\text{nM of H2O2/min/mg of protein} = \frac{\Delta \text{A/min} \times \text{ volume of assay}}{(0.0719 \times \text{ volume of sample } \times \text{ mg of protein })}$$

Estimation of GSH Level. The 125 µL of mammary gland tissue homogenate (10%) was mixed with 100 µL of distilled water and precipitated with 25 µL of TCA (50%). After that, the sample was vortexed for 10 min and centrifuged at 15,000 rpm for 15 min. The supernatant (66 µL) was mixed with 131 µL tris buffer and 3 µL of 5,5′-dithiobis-2-nitrobenzoic acid (11594726, Thermo Fisher Scientific, Waltham, MA, USA). The OD was measured at 405 nm [27,28]. The following formula was used to calculate tissue GSH activity:

$$\text{GSH}(\mu\text{M/mg of protein }) = (310.4 \times \text{Ei} \times \text{OD at } 412 \text{ nm})/\text{mg of protein}$$

where Ei is the correction factor (0.542).

Lactate Assay

The lactate assay was conducted using a kit from Cayman Chemicals (Glycolysis assay kit, 600450, Cayman Chemical, Ann Arbor, MI, USA). Serum samples from each group were assessed for lactate quantification using a microplate reader (SpectraMax ABS Plus, Rochester, NY, USA). The samples were processed following the kit instructions, and calculations were made based on the recorded readings [29].

Statistical Significance

GraphPad Software 8.0.1 (GraphPad Software, Inc., San Diego, CA, USA) was used to evaluate differences between groups for statistical significance. The statistical significance was determined using one-way ANOVA and Tukey's multiple comparison test. Values are shown as mean ± standard deviation (SD). Statistical significance was determined by $*p < 0.05$, $**p < 0.01$, $***p < 0.001$, and $****p < 0.0001$.

Results

In-Silico Study

A library of 67,609 ligands was screened via HTVS and 7011 compounds were extracted against FIH-1 based on Lipinski's Rule of Five to adopt compounds with the physicochemical properties of potential drug-like candidates. The top hits from the HTVS result were passed to another level of the docking module standard precision (SP). The 144 compounds from the SP glide module were extracted and further scrutinized against ADME and toxicity profile. Finally, two compounds BBAP-8 (4-(9,10-dimethoxy-5,11-dioxoisoindolo[2,1-a] quinazolin-6 (5H, 6aH, 11H)-yl)-N-(1H-imidazol-2-yl) butanamide) and BBAP-9 (6-(5,11-dioxoisoindolo[2,1-a]-quinazolin-6(5H,6aH,11H)-yl)-N-(1H-imidazol-2-yl) hexanamide)) were selected based on good docking score, suitable absorption, distribution, metabolism, excretion and toxicity (ADMET) profile, and availability. Both compounds potentially activated FIH-1 when scrutinized through a 2-OG dependent assay. To consider the volume of data, we represent the BBAP-9 compound here. The BBAP-9 exhibited a docking score of –8.162 when docked with FIH-1 (5OP6) (**Supplementary Table 2**). The 2D and 3D dock poses were assessed and depicted in (Fig. 1A,B). The ADME analysis determined that BBAP-9 has good human oral absorption at 85.98%, following Lipinski's rule (Yes, 0 violation) and other attributes that are represented in **Supplementary Table 2.** Thereafter, the oral rat LD50 was estimated to be 1187.92 mg/kg using TEST (**Supplementary Table 3**).

2-OG Dependent in Vitro FIH-1 Assay

The amount of 2-OG in the sample reflects the fluorescence intensity; less fluorescence indicates a lower 2-

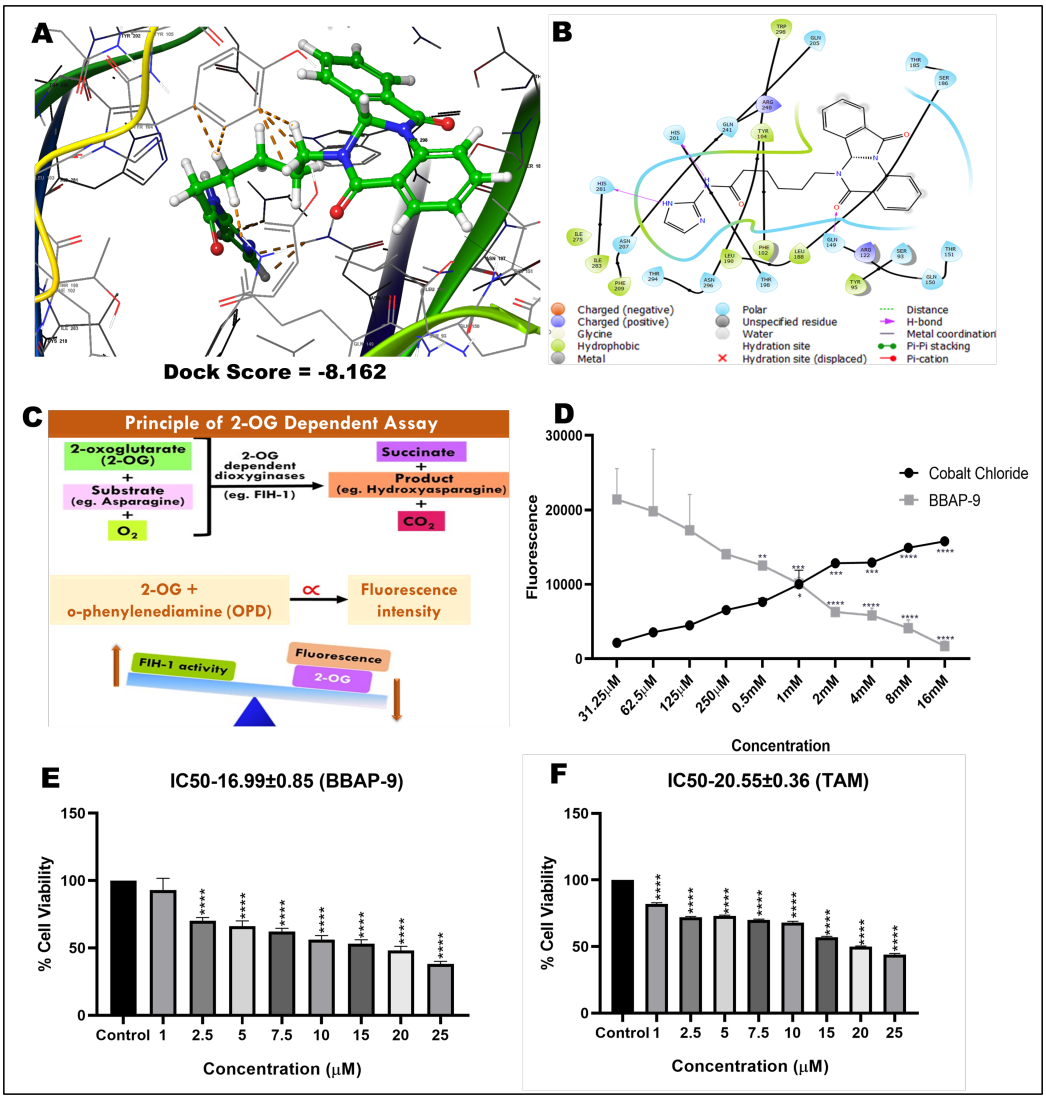

Fig. 1. Molecular docking of BBAP-9, 2-OG dependent and MTT assay. (A) 3D dock pose of BBAP-9 with FIH-1. The BBAP-9 has dock score –8.162, indicating good binding affinity with various amino acid residues Ser 93, Tyr 95, Tyr 104, Gln 149, Gln 150, Leu 188, Leu 190, Thr 198, His 201, His 281, Asn 207, Phe 209, Thr 151, Asn 296, Trp 298. These residues act as binding pockets of BBAP-9. BBAP-9 shows three hydrogen bonds with Gln 149, His 201, and His 281 amino acid residues which also suggest the good binding affinity of BBAP-9 and FIH-1. (B) 2D dock pose of BBAP-9 with FIH-1. (C) Principle of 2-OG dependent assay. The activity of FIH-1 depends on the consumption of 2-OG (substrate of FIH-1). In the reaction mixture, 2-OG and o-phenylenediamine (OPD) give a fluorescent product and release CO_2. The amount of 2-OG present in the samples is closely correlated with fluorescence intensity; less fluorescence indicates less 2-OG level which means increase the activity of FIH-1. (D) The graphical representation shows the result of the 2-OG-dependent assay of FIH-1. Effect of BBAP-9 and cobalt on *in vitro* FIH-1 activity. The result of BBAP-9 shows that FIH-1 is activated in the *in vitro* assay, while cobalt chloride exhibited the vice-versa effect and served as a negative control. The control group was considered as 100% FIH-1 activity. Values are displayed as the Mean ± SD (standard deviation). (E) Assessment of BBAP-9 cytotoxicity on MCF-7 cells. Histogram representation of BBAP-9 against MCF-7 cells using MTT assay. The absorbance was measured at 570 nm. The control group was considered to have 100% cell viability. The BBAP-9 treated cells were compared with the control group. (F) Assessment of cytotoxicity of TAM on MCF-7 cells using MTT assay. A Histogram of TAM represents the cytotoxicity against MCF-7 cells. The reduction in absorbance at 570 nm was determined in a concentration concentration-dependent manner. The cell viability was considered 100% in the control group. Values are displayed as the Mean ± SD. One-way ANOVA is used to compare the groups, and Tukey's multiple comparison test is performed (*$p < 0.05$, **$p < 0.01$, ***$p < 0.001$, ****$p < 0.0001$). BBAP-9, 6-(5,11-dioxoisoindolo [2,1-a] quinazolin-6(5H,6aH,11H)-yl)-N-(1H-imidazol-2-yl) hexanamide; 2-OG, 2-oxoglutarate; MTT, 3-(4,5-dimethylthiazol-2-yl)-2,5-diphenyltetrazolium bromide; FIH-1, factor inhibiting hypoxia-inducible factor-1α; TAM, tamoxifen.

Journal of
BIOLOGICAL REGULATORS
and Homeostatic Agents

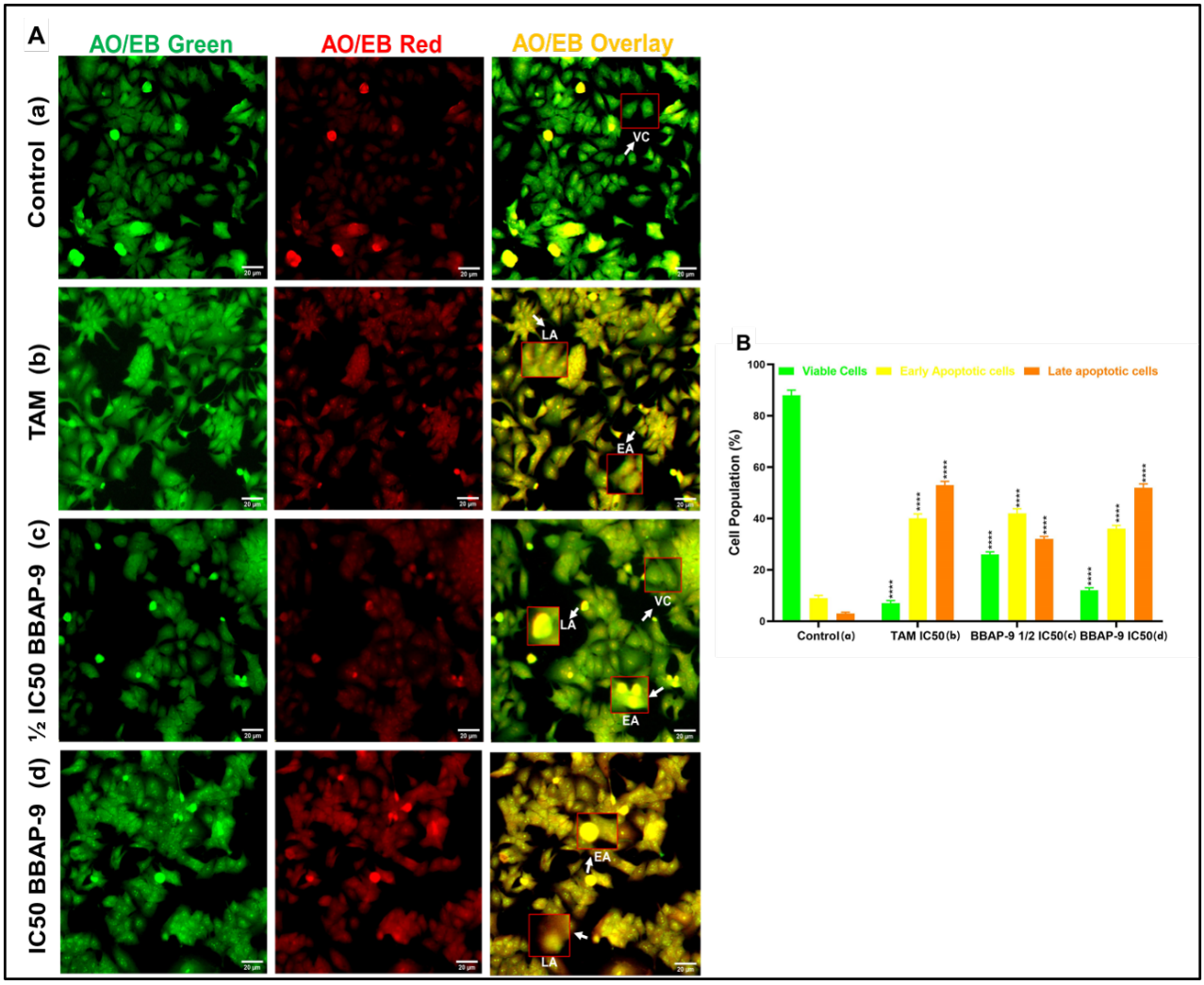

Fig. 2. Effect of BBAP-9 on morphological changes in MCF-7 cells. (A) Fluorescent microscopy images of acridine orange/ethidium bromide (AO/EB) staining at green, red, and merged channels: The effect of BBAP-9 on morphological changes in MCF-7 cells using AO/EB dual labeling (a) control MCF-7 cells, (b) TAM half-maximal inhibitory concentration (IC50), (c) BBAP-9 ½ IC50, and (d) BBAP-9 IC50, respectively. Fluorescence microscopy of stained cells revealed morphological alterations in treated cells compared with control cells. (B) The bar graph represents the effect of BBAP-9 on the percentage of cell population in distinct apoptotic phases. The viable cells show the green colour, early apoptotic cells represent the yellow colour, and late apoptotic cells display the orange colour. Values are displayed as the Mean ± SD. One-way ANOVA was used to compare the groups, and Tukey's multiple comparison test was performed (****$p < 0.0001$). VC, viable cells; EA, early apoptosis; LA, late apoptosis; TAM, tamoxifen. The images were observed under a fluorescence microscope at 20× magnification (scale bar = 20 µm).

OG level (higher FIH-1 activity, 2-OG is a substrate for FIH-1). From the experiment, our results showed that increasing the concentration of BBAP-9 exhibited the fluorescence intensity decreasing simultaneously. On the other hand, the fluorescence intensity increased in the presence of the FIH-1 inhibitor ($COCl_2$), indicating that FIH-1 activity was decreased. Our findings suggest that BBAP-9 increases the activity of FIH-1 by using the 2-OG level in the serum sample which, leads to a decrease in fluorescence intensity. Whereas, the opposite effects were observed in the case of $COCl_2$ (Fig. 1C,D).

In Vitro Study

Cytotoxicity of BBAP-9 on MCF-7 Cells

BBAP-9 drastically reduced the viability of MCF-7 cells in a dose-dependent manner. BBAP-9 showed significant cytotoxicity with a half-maximal inhibitory concentration (IC50) value of 16.9 ± 0.85 µM at 24 h (Fig. 1E). The IC50 value of TAM was found to be 20.55 ± 0.36 µM at 24 h as shown in Fig. 1F.

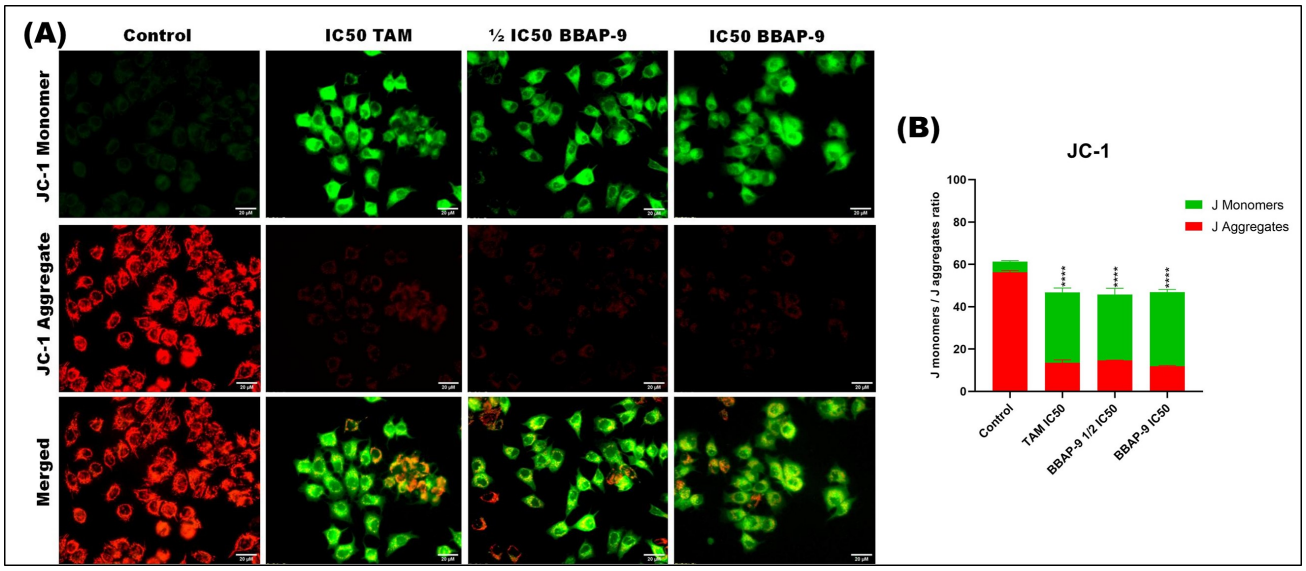

Fig. 3. Effect of BBAP-9 on mitochondrial membrane potential (MMP) using 5,5,6,6′-tetrachloro- 1,1′,3,3′-tetraethylbenzimidazoylcarbocyanine iodide (JC-1) dye in MCF-7 cells. (A) Control, TAM IC50, BBAP-9 ½ IC50, and BBAP-9 IC50 treated cells were detected by JC-1 fluorescent staining. The normal cell has intense MMP, which reflects the red signal. As the MMP decreased, JC-1 could not accumulate and remained in the monomeric form in the cytoplasm, which showed green fluorescence. The treated cells shift from red to green fluorescence intensity compared to control cells, suggesting the induction of apoptotic changes. The images were captured under the fluorescence microscope at 20× magnification (scale bar = 20 μm). (B) The bar graph represents the JC-1 red-green fluorescence signals within the groups. Values are displayed as the Mean ± SD. One-way ANOVA is used to compare the groups, and Tukey's multiple comparison test was performed (****$p < 0.0001$).

Effect of BBAP-9 on Apoptotic Morphological Changes by AO/EB Staining

The apoptotic morphological changes were increased when the cells were treated with TAM and BBAP-9, which appeared yellow and orange coloured in comparison to control cells ($p < 0.0001$), as depicted in Fig. 2. The percentage of viable cells (VC) was markedly decreased by TAM IC50 (8 ± 3.27%), BBAP-9 ½ IC50 (27 ± 3.21%), and BBAP-9 IC50 (12 ± 2.83%) treatments compared with control cells (88 ± 2.86%) ($p < 0.0001$). The TAM IC50, BBAP-9 ½ IC50, and BBAP-9 IC50 treatments contained 40 ± 3.67%, 42 ± 2.89%, and 36 ± 2.85% of the early apoptotic (EA) cells, 53 ± 3.56%, 32 ± 2.23%, and 52 ± 3.27% of the late apoptotic (LA) cells, respectively. These apoptotic modifications were found to be significant in comparison to the control cells ($p < 0.0001$), which contain about 88 ± 2.86% of the VC cells, 7 ± 1.31% of the EA cells, and 3 ± 2.08% of the LA cells. These findings demonstrated that BBAP-9 significantly triggered apoptosis in MCF-7 cells. The percentage of cell death under different apoptotic phases is shown in the bar graph (Fig. 2B).

Measurement of MMP (ψ) Using JC-1 Dye

The control cells showed strong red and weak green fluorescence signals due to high MMP (Fig. 3A,B). The TAM and BBAP-9 treated cells displayed significant loss of red fluorescence and increased green fluorescence signal due to depolarised mitochondria (Fig. 3A,B). The treated cells showed a significant decrease in MMP, as evidenced by a reduction in the red/green fluorescence ratio with both doses of BBAP-9 compared with control cells ($p < 0.0001$) as depicted in the bar graph (Fig. 3B).

In Vivo Study

Hemodynamic Changes

The results were assessed in the form of PLS-DA score, VIP score, and Box-Cum-Whisker plots using the online web server Metaboanalyst.5.0 (https://www.metaboanalyst.ca/). The 2D PLS-DA score plot of normal control and treated groups exhibited substantial separation from DMBA group (Fig. 4A). The ECG parameters were identified from VIP score plot of complete data and resulted in top 15 ECG parameters are shown in increasing order of VIP score values to highlight their discrimination within the groups (Fig. 4B). The Box-cum whisker plots (Fig. 4C) showed that the heart rate (HR), R amplitude, P amplitude, Q amplitude, S amplitude, T amplitude, QRS amplitude, and RR interval were significantly different in normal and treated groups ($p < 0.05$). A significant decrease in HR was observed in DMBA treated animals. It has been reported that the HR reflects the cardiac dysfunction, and the decrease in HR reflects the bradycardia, heart attack, and coronary artery disease. Moreover, the significant prolongation in RR and QRS interval was also observed in DMBA

Journal of
BIOLOGICAL REGULATORS
and Homeostatic Agents

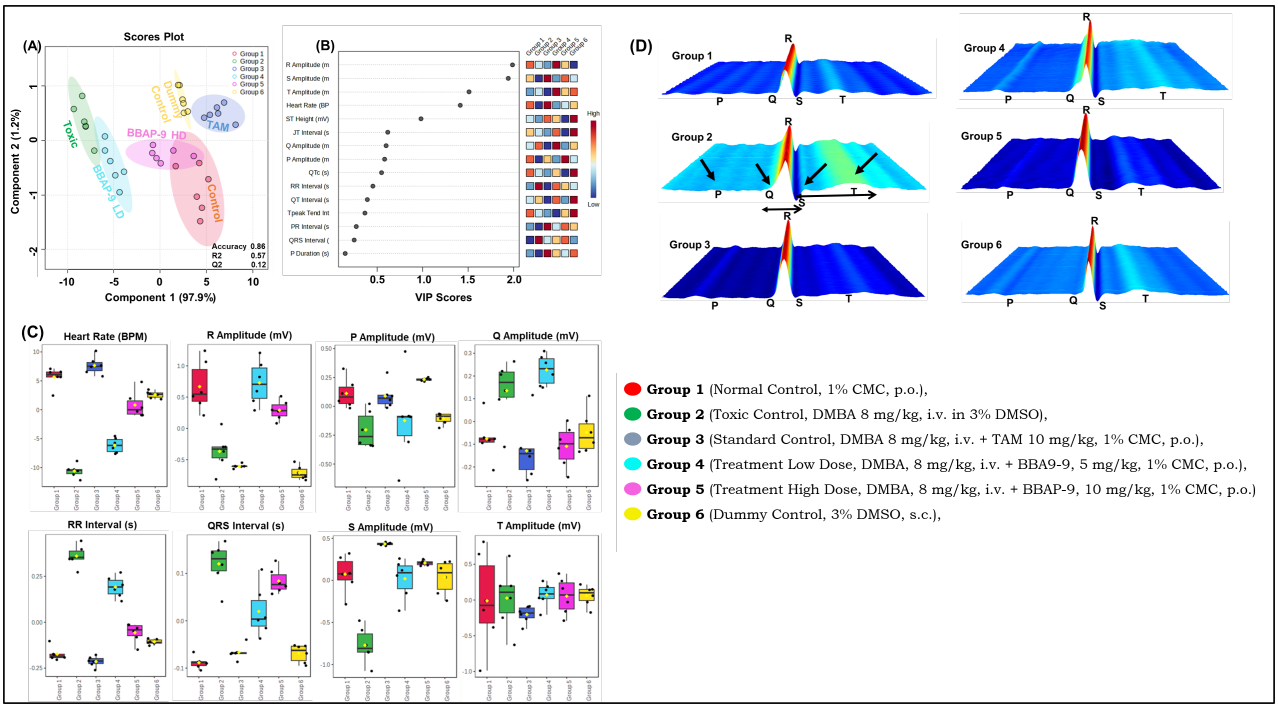

Fig. 4. Effect of BBAP-9 treatment on ECG parameters. (A) The distinct separation of the normal and treated groups is visible in the 2D PLS-DA score plot of ECG parameters. (B) VIP score plot representation of ECG recording with reverse chronological order within the groups. (C) Box-cum whisker plots depicting quantitative changes of autonomic signals in experimental groups. (D) Waterfall plot representation of ECG recording of experimental animals. In the waterfall plot, the total values are indicated in blue, representing the normal ECG signal or waves that fit into the RR interval and beat complexity. It helps to understand how an initial value is affected by a series of positive and negative values, where the red color shows the negative values and the green color shows the positive values. Arrows indicate the abnormalities in the ECG. The DMBA-treated animals exhibited prolonged T amplitude, Q amplitude, ST segment, QRS interval, and decreased P wave compared with the control group. These changes were restored with BBAP-9 treatment. Groups were differentiated as follows: (Group 1) Normal Control (1% carboxy methyl cellulose (CMC), p.o.); (Group 2) Toxic Control (DMBA 8 mg/kg, i.v. in 3% DMSO); (Group 3) Standard Control (DMBA 8 mg/kg, i.v. + TAM, 10 mg/kg, 1% CMC, p.o.); (Group 4) Treatment Low Dose (DMBA 8 mg/kg, i.v. + BBAP-9, 5 mg/kg, 1% CMC, p.o.); (Group 5) Treatment High Dose (DMBA 8 mg/kg, i.v. + BBAP-9, 10 mg/kg, 1% CMC, p.o.); (Group 6) Dummy Control (3% DMSO, s.c.). ECG, electrocardiogram; DMBA, 7,12-dimethylbenz[a]anthracene; TAM, tamoxifen; DMSO, dimethyl sulfoxide.

treated animals. The prolonged RR and QRS interval are important prognostic indicators in patients associated with cardiac failure. The prolonged RR and QRS interval reflect delayed conduction of the SA node which reflects the first-degree AV block and ventricular hypertrophy, respectively. Furthermore, DMBA treated animals showed increased Q and T amplitude which indicates that the patients are at high risk of sudden cardiac death. Based on the above, the DMBA has adverse effects on the heart. The same ECG parameters were restored toward control after BBAP-9 administration with both doses except Q amplitude in low doses (Fig. 4C). The HRV analysis of DMBA treated group showed higher average RR, median RR, and LF and decreased HF and LF/HF ratio compared to the control group. The alteration in these parameters reflects the cardiac abnormalities. After BBAP-9 treatment, the median and average RR significantly returned to normal ($p < 0.0001$), except for the LF, HF, and LF/HF ratio ($p > 0.05$). Meanwhile, the SDRR, SD rate, and SDSD were not significantly altered in our study ($p > 0.05$) (**Supplementary Table 4**). The waterfall plot of the ECG recording was represented within the groups (Fig. 4D). ECG waterfall plot displays a 3D plot of averaged beats. ECG monitors the heart's electrical activity and imparts the valuable information regarding the physiology of heart. The ECG recording of DMBA-treated animals demonstrated significant sinus rhythm alteration which was restored in BBAP-9 treatments. In waterfall plots, color keys indicate the cumulative response of positive and negative values.

Carmine Staining of the Whole Mount Mammary Tissue

In DMBA treated animals, the number of LO, AB, TEB, and DF scores were considerably enhanced, representing more cellular proliferation and differentiation to prompt the mammary gland carcinoma (Fig. 5B). Whereas the normal control group showed a lower number of LO,

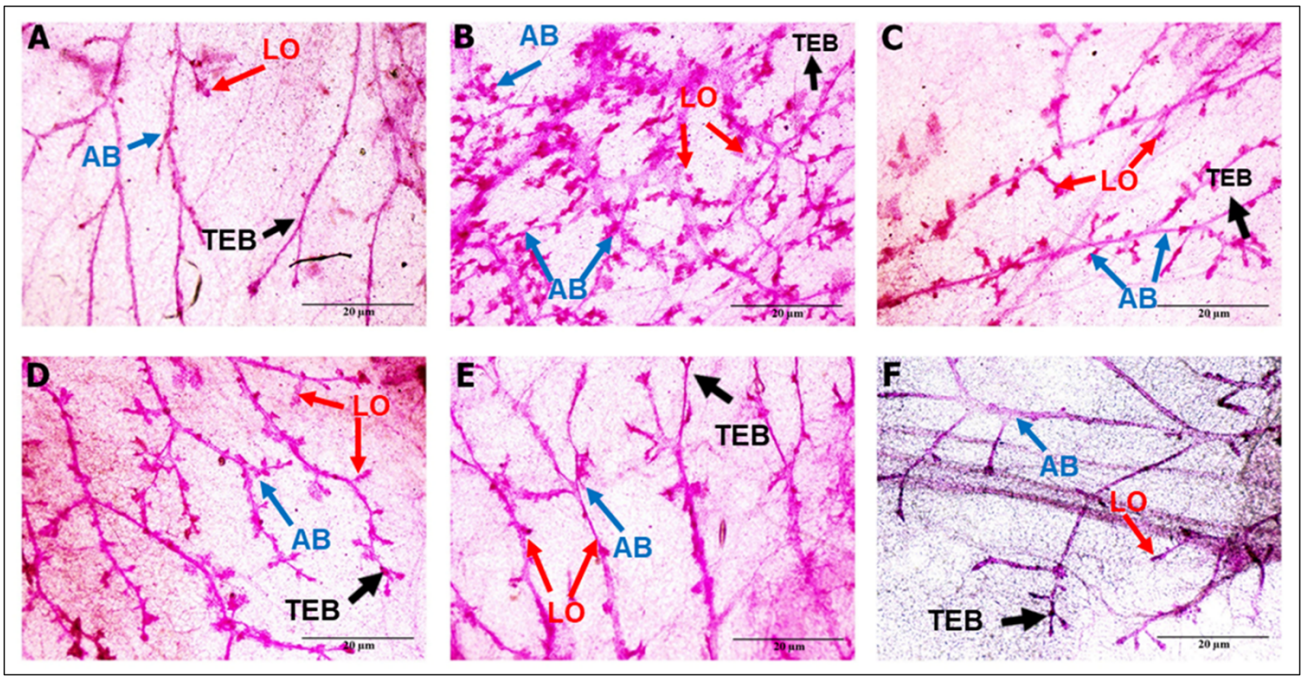

Fig. 5. The anti-proliferative effect of BBAP-9 was determined using carmine staining. Carmine staining was used to examine mammary gland tissue at a microscopic level (10× magnification, scale bar = 20 µm). The blue arrow represents alveolar buds, the black arrow represents terminal end buds, and the red arrow shows lobules. (A) Normal control, and (F) dummy control showed lower AB, LO, TEB, and DF scores, suggesting normal growth of cells. (B) The DMBA-treated group showed significant AB, LO, and TEB branching, indicating increased cell proliferation. (C) A lesser number of AB, LO, and TEB branching was visible in the TAM-treated group. (D,E) BBAP-9 treated groups showed a smaller number of AB, LO, and TEB branching significantly in a dose dose-dependent manner. Groups were differentiated as follows: (Group 1) Normal Control (1% CMC, p.o.); (Group 2) Toxic Control (DMBA 8 mg/kg, i.v. in 3% DMSO); (Group 3) Standard Control (DMBA 8 mg/kg, i.v. + TAM, 10 mg/kg, 1% CMC, p.o.); (Group 4) Treatment Low Dose (DMBA 8 mg/kg, i.v. + BBAP-9, 5 mg/kg, 1% CMC, p.o.); (Group 5) Treatment High Dose (DMBA 8 mg/kg, i.v. + BBAP-9, 10 mg/kg, 1% CMC, p.o.); (Group 6) Dummy Control (3% DMSO, s.c.). AB, alveolar buds; TEB, terminal end buds; LO, lobules; DF, differentiation score.

AB, TEB, and DF scores, indicating normal growth and cell proliferation (Fig. 5A). In BBAP-9 treated animals, the number of LO, AB, TEB, and DF score all considerably returned to normal compared with DMBA treatment ($p < 0.0001$) (Fig. 5D,E). The 3% DMSO-treated animals did not show more cellular proliferation, indicating that this solvent has no morphological consequences (Fig. 5F). TAM therapy was also effective and afforded/provided mammary gland protection against the same (Fig. 5C). In the line of carmine staining, results suggest that the BBAP-9 protected DMBA-treated animals by reducing LO, AB, TEB, and DF scores (Table 1).

Histopathology of the Mammary Gland Tissue

The normal morphology of mammary gland tissue was represented via the normal control group and dummy control group, which showcased the normal lumen size with the intact lining of myoepithelial cells (mec), luminal epithelial cells (lec), adipocytes (ad), and mammary ducts (md) surrounding the reduced fibrous tissue (Fig. 6A,P). The DMBA treated animals revealed degraded mammary ducts (dmd) with periductal stromal fibrosis and fatty tissue (psf), atypical hyperplasia (ah), ad invasion to the adjacent cells, and distorted lec and mec lining of mammary ducts (Fig. 6D). The TAM and BBAP-9 treated groups showed better architectural profile and reduced cellular propagation of mammary tissue, with an ordered distribution of lec, mec, and ad towards normal control compared with the DMBA treated group (Fig. 6G,J,M). The results of H&E staining were emphasized much more through the determination of threshing stained zone followed by pixel versus intensity evaluation using 3D interactive surface plot and logarithmic histogram (Fig. 6B,E,H,K,N,Q and Fig. 6C,F,I,L,O,R, respectively). Based on histological findings, we can say that BBAP-9 treatment at both doses significantly reduced the risk of DMBA-induced mammary gland carcinoma.

Effect of BBAP-9 on Structural Changes Using SEM

The normal control and dummy control animals represented organized breast lobules with a smooth and supple texture, as well as uniformly high density of surface microvilli (mv) (Fig. 7A,P). Whereas, DMBA treated animals

Journal of
BIOLOGICAL REGULATORS
and Homeostatic Agents

Table 1. Effect of BBAP-9 on cellular proliferation in mammary gland tissues.

Groups	AB	TEB	(AB + TEB)	LO	DF (AB + TEB + LO)
Group 1	138.00 ± 2.65****	85.33 ± 5.51****	223.33 ± 5.77****	163.33 ± 4.04****	386.67 ± 7.29****
Group 2	201.33 ± 3.51	140.33 ± 7.64	341.67 ± 4.16	325.67 ± 6.77	667.33 ± 10.59
Group 3	160.66 ± 5.13****	95.67 ± 4.04****	256.33 ± 3.21****	169.33 ± 6.11****	425.66 ± 5.86****
Group 4	179.33 ± 3.06****	116.33 ± 4.73****	295.67 ± 5.69****	261.67 ± 6.03****	557.33 ± 2.08****
Group 5	165.33 ± 4.51****	100.66 ± 5.51****	266.00 ± 6.85****	176.33 ± 6.51****	442.33 ± 4.16****
Group 6	142.67 ± 4.16****	88.33 ± 3.06****	231.00 ± 7.21****	164.00 ± 5.57****	395.00 ± 7.00****

(Values are presented as Mean ± SD), and each group contains 6 animals. Comparisons were made using one-way ANOVA followed by Tukey's multiple test. All groups were compared with the toxic control group (****$p < 0.0001$). (Group 1) Normal Control (1% CMC, p.o.); (Group 2) Toxic Control (DMBA 8 mg/kg, i.v. in 3% DMSO); (Group 3) Standard Control (DMBA 8 mg/kg, i.v. + TAM, 10 mg/kg, 1% CMC, p.o.); (Group 4) Treatment Low Dose (DMBA 8 mg/kg, i.v. + BBAP-9, 5 mg/kg, 1% CMC, p.o.); (Group 5) Treatment High Dose (DMBA 8 mg/kg, i.v. + BBAP-9, 10 mg/kg, 1% CMC, p.o.); (Group 6) Dummy Control (3% DMSO, s.c.). AB, alveolar buds; TEB, terminal end buds; LO, lobules; DF, differentiation score.

represented scattered cellular architecture with distorted membrane ruffles (dmr) and deformed microvillous (dmv) pattern with a pitted epithelial surface (pes) (Fig. 7D). However, BBAP-9 dose dependently and TAM treatments revealed regularized membrane ruffles (rmr), as well as restored microvillous (rmv) over the membrane surface toward normal control (Fig. 7J,M,G). The surface architecture of mammary gland tissues was highlighted much more on the data set of constructs indicating that the score was determined using Image J software (1.53f51, National Institutes of Health, Rockville, MD, USA) by thresh holding zone of SEM images, pixel versus intensity analysis by the 3D interactive surface plot and logarithmic analysis (Fig. 7B,E,H,K,N,Q and Fig. 7C,F,I,L,O,R, respectively). According to surface architectural observations, we can infer that BBAP-9 provided mammary tissue protection by recovering aberrant cellular architecture.

Effect of BBAP-9 on Oxidative Stress Markers

The DMBA treated group significantly increased the level of TBARs in comparison with the normal control group ($p < 0.0001$), which was dose-dependently restored by BBAP-9 treatment. Similarly, the PC level was increased after DMBA treatment, which was significantly decreased after BBAP-9 treatment in dose-dependent manner. After DMBA treatment, the amounts of GSH, SOD, and catalase decreased. Treatment with BBAP-9 restored GSH, SOD, and catalase levels significantly in a dose-dependent way towards normal control compared with DMBA treated animals ($p < 0.0001$). TAM therapy provided antioxidant activity in mammary gland protection against DMBA treated animals. All effects are depicted in the graph shown in Fig. 8A–E.

Effect of BBAP-9 on the Lactate Level

Lactate is a hallmark of cancer growth, which involves various cancer adaptive mechanisms such as angiogenesis, metastasis, cellular metabolism, and immunosurveillance. To consider this, we determined the level of lactate in serum samples. Lactate resulted in a significant increase in DMBA treated animals and restored towards normal control upon BBAP-9 treatment in a dose-dependent manner ($p < 0.0001$) (Fig. 8F). TAM treatment also reduced the lactate level compared with DMBA treated animals.

Discussion

The present study demonstrated the anti-cancer activity of BBAP-9 through the chemical activation of FIH-1. The BBAP-9 was selected based on *in-silico* screening against FIH-1. BBAP-9 activated FIH-1 when scrutinized against 2-OG-dependent *in vitro* assay and further subjected to evaluate its apoptotic and anti-cancer potential using *in vitro* and *in vivo* techniques. BBAP-9 has a potential cytotoxic effect against MCF-7 cells and decreases their viability even at low concentrations compared to TAM. The apoptotic morphological changes were evaluated using AO/EB staining [30]. The BBAP-9 treated cells showed apoptotic morphological features such as early and late apoptotic cells, which appeared yellow and orange color, respectively. BBAP-9 treatments significantly reduced the percentage of healthy cells compared to the control cells. The concomitant treatment of BBAP-9 exhibited a significantly increased percentage of early and late apoptotic cells; which suggests the apoptotic potential of BBAP-9. Moreover, the impact of BBAP-9 on MMP was further confirmed using JC-1 staining, because depolarisation of MMP is a hallmark of apoptosis [31]. The MMP was higher in control cells, where JC-1 dye accumulates within the matrix of the mitochondria in the form of J aggregates and generates red fluorescence. While, JC-1 can not to accumulate within the matrix and remains in monomeric form when cells have lower MMP and display green fluorescence [23,31]. From the findings, the alteration in MMP in the BBAP-9 treated groups is determined by the change in the red-to-green fluorescence ratio, and the declined MMP proves that apoptosis has occurred.

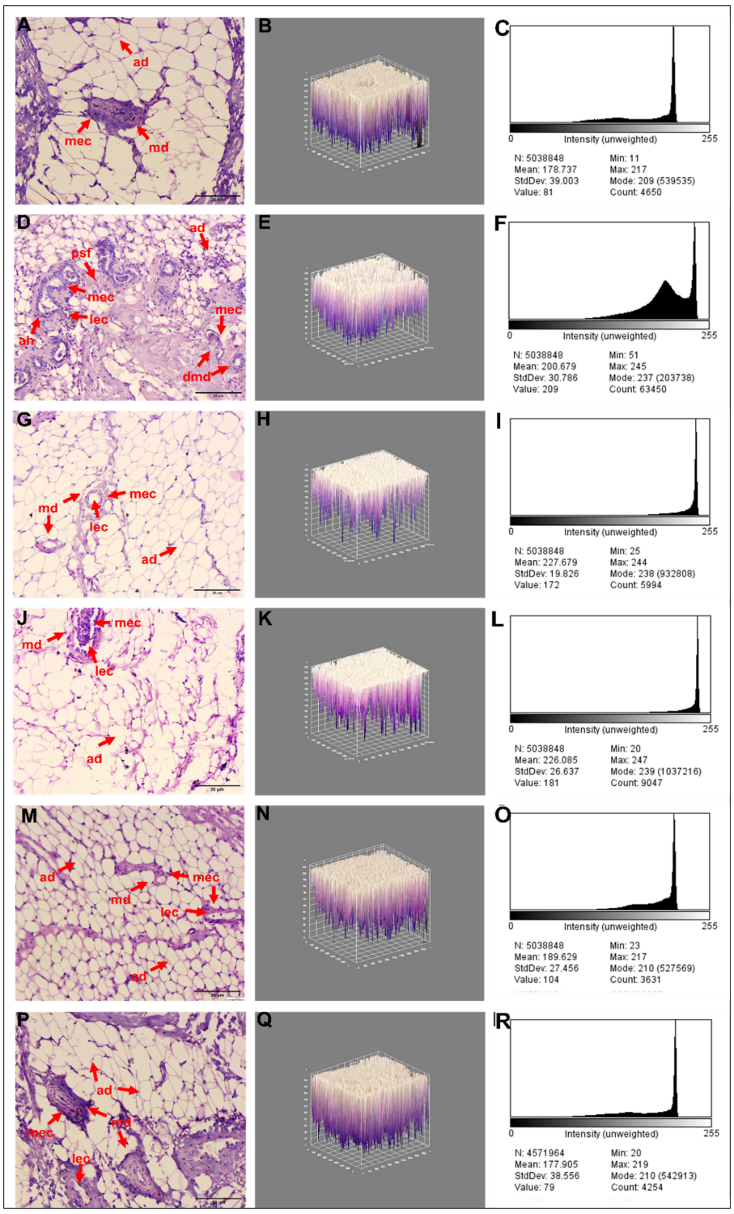

Fig. 6. Effect of BBAP-9 on mammary gland morphology using hematoxylin and eosin (H&E) staining. Mammary gland tissues of the control and dummy control groups (A,P) showed the normal md with intact covering of basement membrane, healthy epithelial lining, and normal distribution of ad. (D) DMBA-treated mammary gland showed degraded md with psf, and there were discontinuous layers of lec, mec, ah, and ad invasion in surrounding cells. Mammary tissue structure was better in the TAM and BBAP-9-treated groups than the DMBA group with the intact basement membrane, with orderly arranged lec, mec, and ad towards normal control in dose-dependent manner, respectively (G,J,M). Digital image analysis of mammary tissues: Using Image J software (1.53f51, National Institutes of Health, Rockville, MD, USA), 3D image reconstruction and software-based analysis dataset of constructs representing score was performed by first threshold holding stained zones of H&E images, then pixel versus intensity determination by the 3D interactive surface plot, and analysing log-histogram (B,E,H,K,N,Q and C,F,I,L,O,R). Groups were differentiated as follows: (Group 1) Normal Control (1% CMC, p.o.); (Group 2) Toxic Control (DMBA 8 mg/kg, i.v. in 3% DMSO); (Group 3) Standard Control (DMBA 8 mg/kg, i.v. + TAM, 10 mg/kg, 1% CMC, p.o.); (Group 4) Treatment Low Dose (DMBA 8 mg/kg, i.v. + BBAP-9, 5 mg/kg, 1% CMC, p.o.); (Group 5) Treatment High Dose (DMBA 8 mg/kg, i.v. + BBAP-9, 10 mg/kg, 1% CMC, p.o.); (Group 6) Dummy Control (3% DMSO, s.c.). The photographs were taken at 10× magnification (scale bar = 20 µm). ad, adipocytes; ah, atypical hyperplasia; md, mammary ducts; dmd, degraded mammary ducts; lec, luminal epithelial cells; mec, myoepithelial cells; psf, periductal stromal fibrosis and fatty tissue.

Journal of
BIOLOGICAL REGULATORS
and Homeostatic Agents

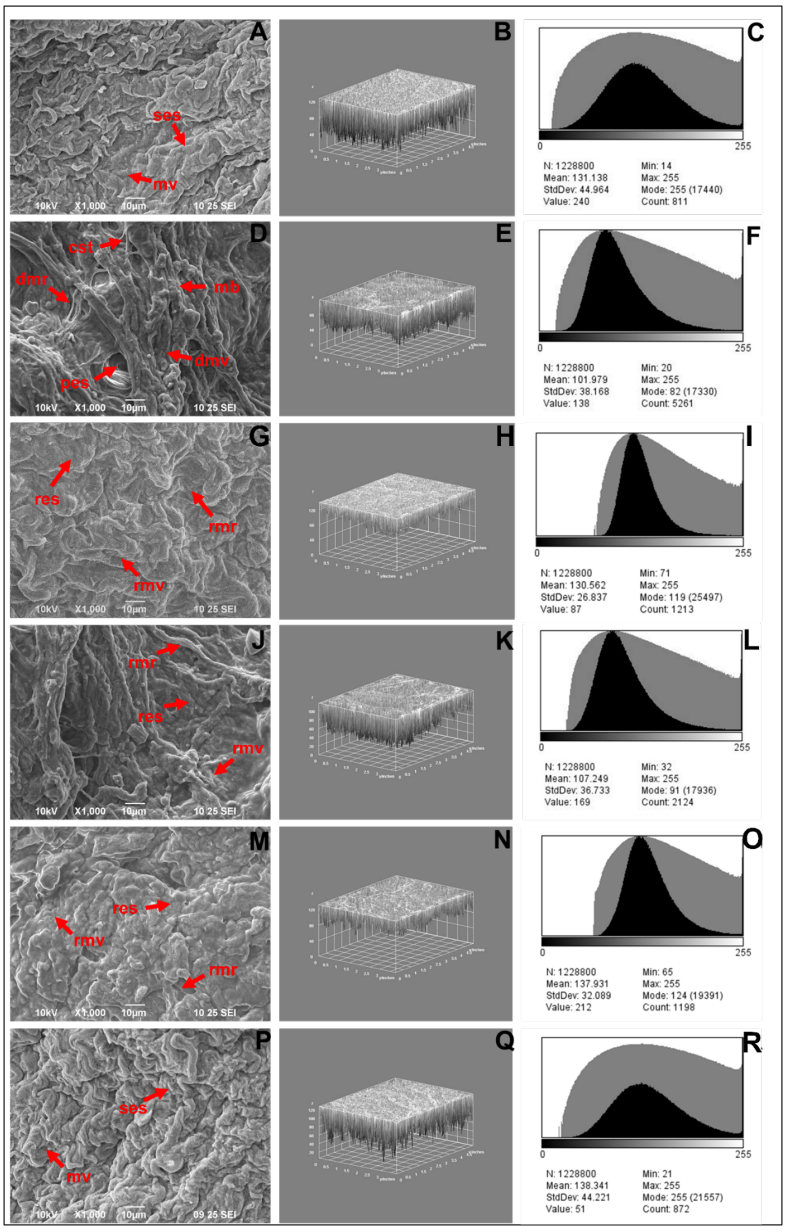

Fig. 7. Effect of BBAP-9 on mammary gland morphology using SEM (Scanning Electron Microscopy) analysis. Mammary gland tissue was analyzed for surface morphological analysis of untreated and treated animals. The normal control and dummy control animals represent the organized breast lobules with smooth, supple texture and a consistently high density of surface mv with apical cytoplasmic membrane (A,P). In contrast, animals treated with DMBA exhibited a dispersed cellular architecture with dmr and dmv with pes (D). However, BBAP-9 (J,M) and TAM (G) treatments showed rmv throughout the membrane surface and rmr in the direction of normal control. The images were taken at 1000× magnification (scale bar = 10 µm). Digital image analysis of mammary tissues: Using Image J software (1.53f51, National Institutes of Health, Rockville, MD, USA), 3D image reconstruction and software-based analysis dataset of constructs representing score was performed, followed by pixel versus intensity determination by the 3D interactive surface plot, and analysing of log-histogram (B,E,H,K,N,Q and C,F,I,L,O,R). Groups were differentiated as follows: (Group 1) Normal Control (1% CMC, p.o.); (Group 2) Toxic Control (DMBA 8 mg/kg, i.v. in 3% DMSO); (Group 3) Standard Control (DMBA 8 mg/kg, i.v. + TAM, 10 mg/kg, 1% CMC, p.o.); (Group 4) Treatment Low Dose (DMBA 8 mg/kg, i.v. + BBAP-9, 5 mg/kg, 1% CMC, p.o.); (Group 5) Treatment High Dose (DMBA 8 mg/kg, i.v. + BBAP-9, 10 mg/kg, 1% CMC, p.o.); (Group 6) Dummy Control (3% DMSO, s.c.). mv, microvilli; ses, smooth epithelial surface; dmr, distorted membrane ruffles; cst, clefted surface territories; mb, membrane blebs; dmv, deformed microvillous pattern; pes, pitted epithelium surface; rmv, restored microvillous; res, regularized epithelial surface; rmr, regularized membrane ruffles.

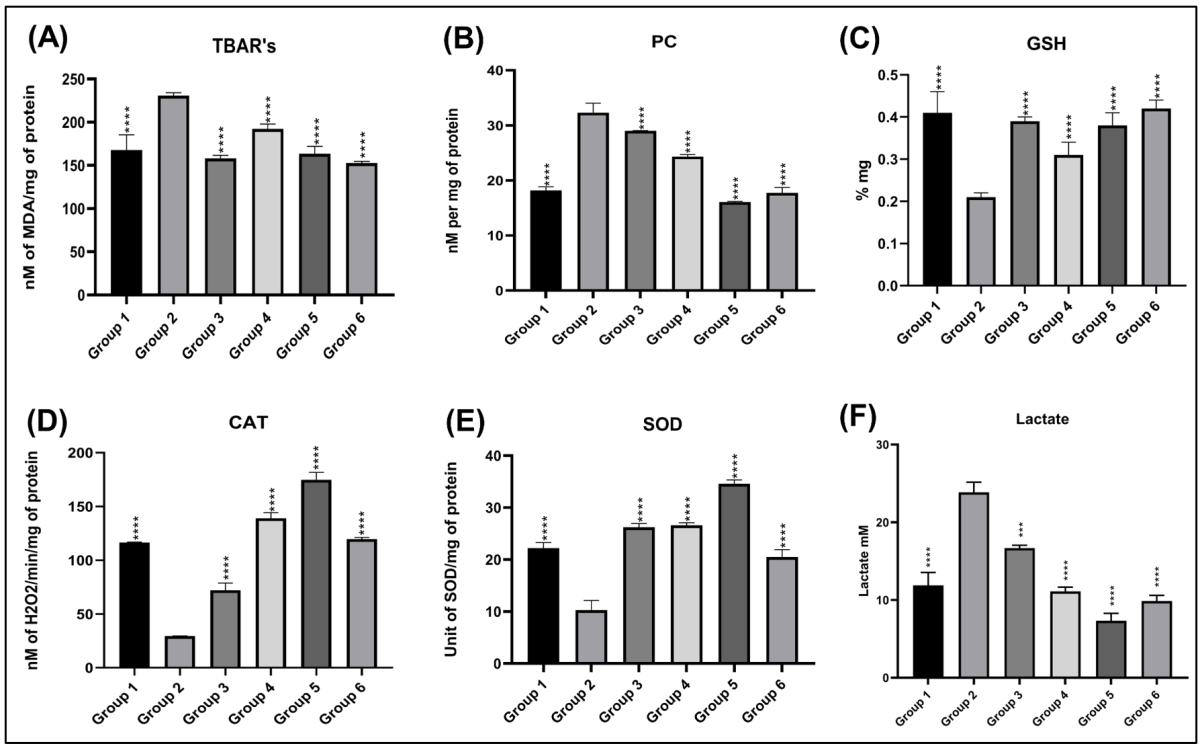

Fig. 8. Effect of BBAP-9 on antioxidant markers and lactate level. Effect of BBAP-9 on the antioxidant markers, inflammatory markers, and lactate level. The bar diagram represents the difference between the control and treated groups. After oral administration of BBAP-9, the levels of thiobarbituric acid reactive substances (TBARs) and protein carbonyl (PC) markedly decreased after being elevated in the DMBA-treated group (A,B). The levels of glutathione (GSH), catalase (CAT), and super oxide dismutase (SOD) decreased after DMBA treatment, which was reset back to normal after BBAP-9 treatment (C–E). The lactate level was significantly increased after DMBA treatment which was restored to normal after BBAP-9 treatment (F). Values are presented as mean ± SD. All groups were compared with the the toxic control group, and comparisons were based on one-way ANOVA, followed by Tukey's multiple comparison test (***$p < 0.001$, ****$p < 0.0001$). Groups were differentiated as follows: (Group 1) Normal Control (1% CMC, p.o.); (Group 2) Toxic Control (DMBA 8 mg/kg, i.v. in 3% DMSO); (Group 3) Standard Control (DMBA 8 mg/kg, i.v. + TAM, 10 mg/kg, 1% CMC, p.o.); (Group 4) Treatment Low Dose (DMBA 8 mg/kg, i.v. + BBAP-9, 5 mg/kg, 1% CMC, p.o.); (Group 5) Treatment High Dose (DMBA 8 mg/kg, i.v. + BBAP-9, 10 mg/kg, 1% CMC, p.o.); (Group 6) Dummy Control (3% DMSO, s.c.).

Based on *in-vitro* findings, BBAP-9 was observed as a FIH-1 activator, and had cytotoxic potential with the ability to trigger apoptosis. Subsequently, the authors expanded their research to assess BBAP-9 *in vivo* efficacy against DMBA-induced mammary gland carcinoma. The DMBA induced mammary gland carcinoma model closely mimics human mammary cancer.

Previous evidence suggests that cancer and chemotherapy-related autonomic dysfunction are prevalent and linked to increased cardiac-associated mortality in cancer patients [32,33]. Therefore, we believed it was worthwhile to assess BBAP-9 impact on ECG and HRV parameters. The DMBA-treated group was visible for autonomic dysfunction via reduced HR and increased in HRV parameters compared to the control group. The results are corroborated with the previous reports [24]. The autonomic dysfunction was dose-dependently eliminated/restored by concomitant administration of BBAP-9.

Thereafter, the efficacy of BBAP-9 was examined to investigate the small proliferative lesions, cellular morphology, and surface architecture of mammary gland tissue using carmine staining, histopathology, and SEM. HIF-1α stimulates the formation of small blood vessels in solid tumors to fulfill the requirements of nutrients and oxygen to the fastly dividing cancerous cells [9]. In the present study, excessive cellular proliferation was observed after DMBA treatment as represented by an increase in the number of LO, AB, TEB, and DF scores, which is in corroboration with the antecedent reports [24,27]. BBAP-9 treatment decreased the number of LO, AB, TEB, and DF scores in a dose-dependent manner, suggesting the antiproliferative potential of BBAP-9. To validate the results of carmine staining, the histopathological changes, and SEM evaluation were also scrutinized. The deterioration of md, lec, mec, ah, and ad invasion in surrounding cells has been described in the histology of mammary gland tissues in DMBA treated animals [24,27]. In the current

Journal of
BIOLOGICAL REGULATORS
and Homeostatic Agents

study, DMBA-treated animals exhibited these aberrant effects, and BBAP-9 therapy significantly curtailed towards normal control. The SEM analysis of DMBA-treated animals showed scattered cellular architecture with distorted mr and deformed mv patterns with pitted epithelial surfaces [34]. The concomitant administration of BBAP-9 showed reasonable restoration of mr and mv. BBAP-9 treatments regularized the cellular proliferation, surface architecture, and membrane ruffles. Based on the above discussed microscopical parameters the authors would like to pertinent the protective effect of BBAP-9 treatment against mammary gland carcinoma.

Reactive oxygen species (ROS) are produced primarily by oxidative stress, linked to mammary gland carcinoma development and the suppression of antioxidant enzymes that fight cancer [35]. According to previous studies, oxidative stress and the antioxidant system are altered during the development of mammary gland carcinoma [35,36]. The current study demonstrated the substantial association between them and the progression of cancer, which is intensely evaluated by variations in the oxidative stress markers. Cancer triggers peroxidation of the lipids and proteins in mammary gland tissues. A persistent lipid peroxidation biomarker is malondialdehyde (MDA), and protein carbonyl (PC) is a protein peroxidation biomarker [37]. In the current study, the MDA and PC levels in the DMBA-treated group increased, and these levels were subsequently restored to normal by the administration of BBAP-9. It would be appropriate to point out that BBAP-9 therapy decreased TBARs and PC levels while balancing the antioxidant defence offered by SOD, catalase, and GSH.

Lactate is an oncometabolite observed in the tumor microenvironment of solid tumors [38]. Studies suggest that it initiates cancer growth signaling by promoting angiogenesis, metastasis, and glycolysis. The BBAP-9 treatment effectively decreased the level of lactate compared to DMBA treated animals, which suggests BBAP-9 is a promising potential candidate in cancer therapeutics against mammary gland carcinoma [38–40].

Conclusions

In conclusion, the current study's findings demonstrate that BBAP-9 has potential cytotoxic activity and induced apoptosis significantly in MCF-7 cells, which was confirmed using AO/EB and JC-1 stainings. Moreover, BBAP-9 has chemotherapeutic efficacy on DMBA-induced mammary gland carcinoma in animals and this can be attributed to its propensity to enhance antioxidant profiles and inhibit cellular proliferation, improve surface architecture, soothing membrane ruffles, and decrease the lactate effects. Thus, we postulated that BBAP-9 may be a novel FIH-1 activator in mammary gland carcinoma. More research is needed to explore the underlying molecular mechanisms to demonstrate the efficacy of BBAP-9 as an anticancer drug.

Availability of Data and Materials

All data included in this study are available from the corresponding author upon request.

Author Contributions

Material preparation and the experiments were performed by SR. Data collection and analysis were performed by MA and AS. GK perceived the idea, designed and supervised the whole study, and prepared and proofread the final manuscript. The first draft of manuscript was written by SR and all authors commented on previous versions of the manuscript. All authors contributed to editorial changes in the manuscript. All authors read and approved the final manuscript. All authors have participated sufficiently in the work and agreed to be accountable for all aspects of the work.

Ethics Approval and Consent to Participate

The animal study was reviewed and approved by the Committee for Control and Supervision of Experiments on Animals (CCSEA) (Approval No. UIP/IAEC/Nov.-2019/13).

Acknowledgment

The authors kindly acknowledge the Department of Pharmaceutical Sciences, Babasaheb Bhimrao Ambedkar University for providing the necessary infrastructure.

Funding

This work is supported by Indian Council of Medical Research, New Delhi, India funding agency to provide the SRF fellowship to SR (ICMR-SRF 2019-6877, Award letter number 3/2/2/121/2019/NCD-III).

Conflict of Interest

The authors declare no conflict of interest.

Supplementary Material

Supplementary material associated with this article can be found, in the online version, at https://doi.org/10.23812/j.biol.regul.homeost.agents.20243805.330.

References

[1] Mehrotra R, Yadav K. Breast cancer in India: Present scenario and the challenges ahead. World Journal of Clinical Oncology. 2022; 13: 209–218.

[2] Muz B, de la Puente P, Azab F, Azab AK. The role of hypoxia in cancer progression, angiogenesis, metastasis, and resistance to therapy. Hypoxia (Auckland, N.Z.). 2015; 3: 83–92.

[3] Yong L, Tang S, Yu H, Zhang H, Zhang Y, Wan Y, *et al*. The role of hypoxia-inducible factor-1 alpha in multidrug-resistant breast cancer. Frontiers in Oncology. 2022; 12: 964934.
[4] McAleese CE, Choudhury C, Butcher NJ, Minchin RF. Hypoxia-mediated drug resistance in breast cancers. Cancer Letters. 2021; 502: 189–199.
[5] Young SD, Marshall RS, Hill RP. Hypoxia induces DNA overreplication and enhances metastatic potential of murine tumor cells. Proceedings of the National Academy of Sciences of the United States of America. 1988; 85: 9533–9537.
[6] Vaupel P. Hypoxia and aggressive tumor phenotype: implications for therapy and prognosis. The Oncologist. 2008; 13: 21–26.
[7] Dengler VL, Galbraith M, Espinosa JM. Transcriptional regulation by hypoxia inducible factors. Critical Reviews in Biochemistry and Molecular Biology. 2014; 49: 1–15.
[8] Wu Y, Li Z, McDonough MA, Schofield CJ, Zhang X. Inhibition of the Oxygen-Sensing Asparaginyl Hydroxylase Factor Inhibiting Hypoxia-Inducible Factor: A Potential Hypoxia Response Modulating Strategy. Journal of Medicinal Chemistry. 2021; 64: 7189–7209.
[9] Rani S, Roy S, Singh M, Kaithwas G. Regulation of Transactivation at C-TAD Domain of HIF-1α by Factor-Inhibiting HIF-1α (FIH-1): A Potential Target for Therapeutic Intervention in Cancer. Oxidative Medicine and Cellular Longevity. 2022; 2022: 2407223.
[10] Singh M, Devi U, Roy S, Gupta PS, Kaithwas G. Chemical activation of prolyl hydroxylase-2 by BBAP-1 down regulates hypoxia inducible factor-1α and fatty acid synthase for mammary gland chemoprevention. RSC Advances. 2018; 8: 12848–12860.
[11] Devi U, Singh M, Roy S, Tripathi AC, Gupta PS, Saraf SK, *et al*. PHD-2 activation: a novel strategy to control HIF-1α and mitochondrial stress to modulate mammary gland pathophysiology in ER+ subtype. Naunyn-Schmiedeberg's Archives of Pharmacology. 2019; 392: 1239–1256.
[12] Devi U, Singh M, Roy S, Gupta PS, Ansari MN, Saeedan AS, *et al*. Activation of prolyl hydroxylase-2 for stabilization of mitochondrial stress along with simultaneous downregulation of HIF-1α/FASN in ER + breast cancer subtype. Cell Biochemistry and Function. 2019; 37: 216–227.
[13] Shin DH, Chun YS, Lee DS, Huang LE, Park JW. Bortezomib inhibits tumor adaptation to hypoxia by stimulating the FIH-mediated repression of hypoxia-inducible factor-1. Blood. 2008; 111: 3131–3136.
[14] Li SH, Shin DH, Chun YS, Lee MK, Kim MS, Park JW. A novel mode of action of YC-1 in HIF inhibition: stimulation of FIH-dependent p300 dissociation from HIF-1α. Molecular Cancer Therapeutics. 2008; 7: 3729–3738.
[15] Yeo EJ, Ryu JH, Cho YS, Chun YS, Huang LE, Kim MS, *et al*. Amphotericin B blunts erythropoietin response to hypoxia by reinforcing FIH-mediated repression of HIF-1. Blood. 2006; 107: 916–923.
[16] Natarajan V, Ramanathan P, Gopisetty G, Ramachandran B, Thangarajan R, Kesavan S. In silico and in vitro screening of small molecule Inhibitors against SYT-SSX1 fusion protein in synovial sarcoma. Computational Biology and Chemistry. 2018; 77: 36–43.
[17] Madhavaram M, Nampally V, Gangadhari S, Palnati MK, Tigulla P. High-throughput virtual screening, ADME analysis, and estimation of MM/GBSA binding-free energies of azoles as potential inhibitors of *Mycobacterium tuberculosis* H37Rv. Journal of Receptor and Signal Transduction Research. 2019; 39: 312–320.
[18] Kalirajan R, Iniyavan K, Rathika G, Pandiselvi A. Molecular docking studies, in-silico ADMET screening, MM-GBSA binding free energy of some novel chalcone substituted 9-anilinoacridines as topoisomerase II inhibitors. International Journal of Computational Biology and Drug Design. 2020; 13: 347–358.
[19] McNeill LA, Bethge L, Hewitson KS, Schofield CJ. A fluorescence-based assay for 2-oxoglutarate-dependent oxygenases. Analytical Biochemistry. 2005; 336: 125–131.
[20] Nakashima Y, Brewitz L, Tumber A, Salah E, Schofield CJ. 2-Oxoglutarate derivatives can selectively enhance or inhibit the activity of human oxygenases. Nature Communications. 2021; 12: 6478.
[21] Roy S, Singh M, Sammi SR, Pandey R, Kaithwas G. ALA-mediated biphasic downregulation of α-7nAchR/HIF-1α along with mitochondrial stress modulation strategy in mammary gland chemoprevention. Journal of Cellular Physiology. 2019; 234: 4015–4029.
[22] Baharara J, Namvar F, Ramezani T, Mousavi M, Mohamad R. Silver nanoparticles biosynthesized using Achillea biebersteinii flower extract: apoptosis induction in MCF-7 cells via caspase activation and regulation of Bax and Bcl-2 gene expression. Molecules (Basel, Switzerland). 2015; 20: 2693–2706.
[23] Roy S, Rawat AK, Sammi SR, Devi U, Singh M, Gautam S, *et al*. Alpha-linolenic acid stabilizes HIF-1 α and downregulates FASN to promote mitochondrial apoptosis for mammary gland chemoprevention. Oncotarget. 2017; 8: 70049–70071.
[24] Singh L, Roy S, Kumar A, Rastogi S, Kumar D, Ansari MN, *et al*. Repurposing Combination Therapy of Voacamine With Vincristine for Downregulation of Hypoxia-Inducible Factor-1α/Fatty Acid Synthase Co-axis and Prolyl Hydroxylase-2 Activation in ER+ Mammary Neoplasia. Frontiers in Cell and Developmental Biology. 2021; 9: 736910.
[25] Keshari AK, Singh AK, Kumar U, Raj V, Rai A, Kumar P, *et al*. 5H-benzo[h]thiazolo[2,3-b]quinazolines ameliorate NDEA-induced hepatocellular carcinogenesis in rats through IL-6 downregulation along with oxidative and metabolic stress reduction. Drug Design, Development and Therapy. 2017; 11: 2981–2995.
[26] Yoshida H, Yoshida A, Fukunishi R, Nagato T, Uehara Y. Scanning electron microscopy of 7,12-dimethylbenz(a)-anthracene-induced mammary carcinoma in the female Sprague-Dawley rat. Virchows Archiv. B, Cell Pathology Including Molecular Pathology. 1980; 32: 105–108.
[27] Gautam S, Rani S, Aldossary SA, Saeedan AS, Ansari MN, Kaithwas G. Effects of phenidone (DuCLOX-2/5 inhibitor) against N-methyl-N-nitrosourea induced mammary gland carcinoma in albino rats. Toxicology and Applied Pharmacology. 2018; 351: 57–63.
[28] Keshari AK, Kumar G, Kushwaha PS, Bhardwaj M, Kumar P, Rawat A, *et al*. Isolated flavonoids from Ficus racemosa stem bark possess antidiabetic, hypolipidemic and protective effects in albino Wistar rats. Journal of Ethnopharmacology. 2016; 181: 252–262.
[29] Gómez de Cedrón M, Acín Pérez R, Sánchez-Martínez R, Molina S, Herranz J, Feliu J, *et al*. MicroRNA-661 modulates redox and metabolic homeostasis in colon cancer. Molecular Oncology. 2017; 11: 1768–1787.
[30] Haridevamuthu B, Manjunathan T, Wilson Alphonse CR, Kumar RS, Thanigaivel S, Chandra Kishore S, *et al*. Functionalized Sulfur-Containing Heterocyclic Analogs Induce Sub-G1 Arrest and Apoptotic Cell Death of Laryngeal Carcinoma In Vitro. Molecules (Basel, Switzerland). 2023; 28: 1856.
[31] Liu SM, Ou SY, Huang HH. Green tea polyphenols induce cell death in breast cancer MCF-7 cells through induction of cell cycle arrest and mitochondrial-mediated apoptosis. Journal of Zhejiang University. Science. B. 2017; 18: 89–98.
[32] Coumbe BGT, Groarke JD. Cardiovascular Autonomic Dys-

Journal of
BIOLOGICAL REGULATORS
and Homeostatic Agents

function in Patients with Cancer. Current Cardiology Reports. 2018; 20: 69.

[33] Teng AE, Noor B, Ajijola OA, Yang EH. Chemotherapy and Radiation-Associated Cardiac Autonomic Dysfunction. Current Oncology Reports. 2021; 23: 14.

[34] Mani G, Arumugam M, Maril A, Devaki T. Naringin attenuates DMBA-induced mammary carcinogenesis in rats via regulating the oxidative stress and antioxidants status. Journal of Chemical and Pharmaceutical Research. 2018; 10: 44–54.

[35] Rahal A, Kumar A, Singh V, Yadav B, Tiwari R, Chakraborty S, *et al*. Oxidative stress, prooxidants, and antioxidants: the interplay. BioMed Research International. 2014; 2014: 761264.

[36] Nourazarian AR, Kangari P, Salmaninejad A. Roles of oxidative stress in the development and progression of breast cancer. Asian Pacific Journal of Cancer Prevention: APJCP. 2014; 15: 4745–4751.

[37] Gautam S, Rawat AK, Sammi SR, Roy S, Singh M, Devi U, *et al*. DuCLOX-2/5 Inhibition Attenuates Inflammatory Response and Induces Mitochondrial Apoptosis for Mammary Gland Chemoprevention. Frontiers in Pharmacology. 2018; 9: 314.

[38] Rastogi S, Mishra SS, Arora MK, Kaithwas G, Banerjee S, Ravichandiran V, *et al*. Lactate acidosis and simultaneous recruitment of TGF-β leads to alter plasticity of hypoxic cancer cells in tumor microenvironment. Pharmacology & Therapeutics. 2023; 250: 108519.

[39] Swetha N, Senghor KA, Ramachandran K. Serum lactate dehydrogenase and lipid profile in breast cancer. International Journal of Pharmacy and Biological Sciences. 2013; 3: 423–432.

[40] Hussien R, Brooks GA. Mitochondrial and plasma membrane lactate transporter and lactate dehydrogenase isoform expression in breast cancer cell lines. Physiological Genomics. 2011; 43: 255–264.